Small

NANO · MICRO small
www.small-journal.com

RESEARCH ARTICLE OPEN ACCESS

Molecular-Level Engineered Approach Induces Built-in Electric Field Modulation in G-C_3N_4/$CoMoS_2$ Heterojunction for Enhanced Hydrogen Generation via Urea Oxidation

Boka Fikadu Banti[1] | Birhanu Bayissa Gicha[2] | Mahendra Goddati[2,3] | Hyojin Kang[4] | Indra Memdi Khoris[2] | Cheru Fekadu Molla[1] | Sohrab Asgaran[5] | Michael Giersig[6] | Njemuwa Nwaji[6] | Jaebeom Lee[1,2,3]

[1]Department of Chemistry, Chungnam National University, Daejeon, Republic of Korea | [2]Research Institute of Materials Chemistry, Chungnam National University, Daejeon, South Korea | [3]Department of Chemical Engineering and Applied Chemistry, Chungnam National University, Daejeon, Republic of Korea | [4]Institute For Sciences of the Universe, Chungnam National University, Daejeon, Republic of Korea | [5]Helmaco Sp. Z o.o. Company, Warszawa, Poland | [6]Institute of Fundamental Technological Research, Polish Academy of Sciences, Warsaw, Poland

Correspondence: Njemuwa Nwaji (nnwaji@ippt.pan.pl) | Jaebeom Lee (nanoleelab@cnu.ac.kr)

Received: 27 February 2026 | **Revised:** 14 April 2026 | **Accepted:** 8 May 2026

Keywords: built-in electric field | electrolysis | heterojunction | hydrogen production | urea oxidation

ABSTRACT

Urea-assisted electrolysis boosts hydrogen production by substituting the sluggish oxygen evolution reaction (OER) with the energetically favorable urea oxidation reaction (UOR), thereby lowering energy consumption. Rational heterojunction engineering modulates charge distribution and generates abundant active sites, facilitating urea adsorption and C—N bond cleavage. Herein, we report a facile electrodeposition strategy to construct g-C_3N_4/$CoMoS_2$ hybrid electrocatalysts. The built-in electric field at the heterojunction creates electrophilic regions on g-C_3N_4 and nucleophilic regions on $CoMoS_2$, selectively activating urea and promoting rapid bond cleavage. Anchoring g-C_3N_4 onto $CoMoS_2$ enables remarkable bifunctional activity toward both UOR and HER, achieving potentials of 1.27 V vs. RHE in 1 M KOH + 0.33 M urea and -80 mV vs. RHE in 1 M KOH at 10 mA cm^{-2}, respectively. Density functional theory (DFT) calculations reveal that interfacial electron transfer enriches $CoMoS_2$ with electrons and depletes g-C_3N_4, enhancing charge transfer, optimizing urea adsorption, and lowering reaction energy barriers. Notably, the g-C_3N_4/$CoMoS_2$//g-C_3N_4/$CoMoS_2$ cell delivers 10 mA cm^{-2} at 1.34 V with excellent stability, demonstrating superior efficiency. This work provides a rational framework for designing efficient, energy-saving urea-assisted hydrogen production systems and reveals how intrinsic electric fields can precisely control charge distribution during catalysis.

1 | Introduction

Hydrogen (H_2) is widely regarded as a promising carbon-neutral energy carrier due to its high gravimetric energy density and environmental benignity [1, 2]. Electrocatalytic water splitting provides a sustainable route for H_2 production; however, its efficiency is hindered by the sluggish kinetics and high overpotential (>1.23 V) of the anodic oxygen evolution reaction (OER), which leads to substantial energy losses [3, 4]. To overcome this limitation, replacing the OER with the anodic oxidation of small molecules such as methanol [5–7], 5-hydroxymethylfurfural [8, 9], ethanol [10–13], hydrazine [14, 15], and urea [16–18] has garnered significant attention as an energy-efficient alternative. Among these, the urea oxidation

is particularly attractive owing to its low theoretical potential (0.37 V vs. RHE), dual functionality in both energy generation and wastewater remediation, and natural abundance of urea [19–23]. Electrocatalysts capable of driving hydrogen production through the UOR hold significant promise for environmental cleanup, simultaneously enabling efficient energy conversion and pollutant removal [24, 25].

Notwithstanding this benefit, the six-electron-transfer nature of UOR engenders intrinsically sluggish kinetics, thereby necessitating the judicious conceptualization of catalysts that are both highly active and durable. Noble metal oxides such as RuO_2 and IrO_2 exhibit benchmark performance for both OER and UOR, but their high cost and scarcity limit large-scale deployment [26–28]. As a result, research has focused on low-cost, non-noble-metal catalysts capable of efficiently driving both UOR and the HER, offering simplified system designs with reduced energy and material requirements. Current design approaches for developing non-precious metal catalysts are generally based on transition metals such as Ni, Co, Fe, etc., through the incorporation of non-metallic elements, including oxygen [29], selenium [29], nitrogen [30, 31], phosphorus [32, 33], and sulfur [34], etc., to optimize catalytic activity. Emerging insights into the mechanism of UOR have resulted in guided design approaches such as heterostructure construction [35–38], elemental doping [39–41], compositional regulation [42], defect engineering [43–45], doping-induced reconstruction [46], and phase engineering [47], to boost electrocatalytic efficiency. The fundamental basis of electrocatalytic activity is surface adsorption-desorption and electron-transfer dynamics. This makes modulating the electronic structure of surfaces, particularly through heterojunction engineering, an effective strategy for enhancing catalytic performance [48]. Heterojunction interfaces induce lattice and electronic-state modulation [35, 36], in which energy-level offsets generate internal electric fields that redistribute charge and stabilize complementary electrophilic and nucleophilic sites [49]. For instance, Ni et al. [50] developed $NiSe_2/FeSe_2$ p–p heterojunctions, where the interfacial built-in electric field accelerates charge transfer and induces local charge redistribution, enhancing intermediate adsorption and achieving 50 mA cm^{-2} at an overpotential of just 127 mV, surpassing both analogous materials and commercial RuO_2. Similarly, He et al. [51] reported a heterojunction catalyst with enriched lattice defects and uniform interfaces, enhancing active site density, electron transfer, and surface area. In a UOR//HER system, it achieved 100 mA cm^{-2} at 1.453 V, 186 mV lower than the OER//HER system, while maintaining excellent durability in 1.0 M KOH/0.5 M urea. These studies highlight the effectiveness of heterojunction architectures in boosting UOR efficiency, although most fabrication methods rely on high temperatures or complex procedures.

Herein, we present a facile and cost-effective approach for constructing a g-$C_3N_4/CoMoS_2$ heterojunction with a built-in electric field through an environmentally friendly electrodeposition method. The electrode catalyst involves the in situ growth of a free-standing $CoMoS_2$ array on nickel foam (NF), followed by the anchoring of ultrathin g-C_3N_4 nanosheets on the $CoMoS_2$ arrays, forming an intimate heterointerface where the intrinsic band offset induces a spontaneous internal electric field. The spatial distribution of positive and negative charges is precisely modulated by the in-built electric field at the heterojunction interface, thereby inducing the formation of electrophilic and nucleophilic domains. These positive and negative complementary regions exhibit strong adsorption toward the electron-donating and electron-withdrawing groups of urea molecules through electrostatic interactions, facilitating the cleavage of the C—N bond and the decomposition of urea.

First-principles DFT calculations reveal work functions (**Φ**) of 4.25 eV (g-C_3N_4) and 5.11 eV ($CoMoS_2$), confirming electron transfer from g-C_3N_4 to $CoMoS_2$ and validating the formation of an internal electric field that enhances both UOR and HER kinetics. These theoretical analyses provide key mechanistic insights and actionable design principles for tailoring interfacial properties. Collectively, the study establishes a robust framework for advancing urea-assisted hydrogen generation with reduced energy requirements and improved catalytic efficacy, offering a viable pathway for next-generation energy conversion systems.

2 | Results and Discussion

2.1 | Synthesis and Structural Characterization of G-C_3N_4/$CoMoS_2$ Heterojunction

The g-$C_3N_4/CoMoS_2$ heterojunction was synthesized through a rational two-step strategy, as illustrated in Figure 1a. Initially, graphitic carbon nitride (g-C_3N_4) nanosheets (Figure S1) were prepared through direct thermal polymerization, while $CoMoS_2$ nanorod arrays were grown in situ on nickel foam (NF) via a straightforward hydrothermal process. Subsequently, g-C_3N_4 nanosheets were uniformly anchored onto the $CoMoS_2$ nanorods through a potentiostatic electrodeposition, yielding the g-$C_3N_4/CoMoS_2$ heterojunction with significantly enhanced catalytic performance. The choice of electrodeposition arises from its simplicity, versatility, cost-effectiveness, and efficiency. It is noteworthy that electrodeposition for one and two cycles results in incomplete nanorod coverage, whereas four cycles lead to pronounced aggregation (Figure S4), hindering electrolyte transport and compromising performance. Consequently, three electrodeposition cycles yield optimal performance. Detailed experimental procedures for catalyst synthesis are provided in the Experimental Section. The morphology of g-$C_3N_4/CoMoS_2$ and the individual components was systematically characterized by scanning electron microscopy (SEM) and transmission electron microscopy (TEM).

Figure 1b presents the SEM image of $CoMoS_2$, revealing well-defined, vertically oriented nanorod structures uniformly anchored to the NF substrate. Furthermore, Figure S2 presents SEM and TEM images at various magnifications, along with the corresponding elemental mapping of the $CoMoS_2$ nanorod. As shown in Figure 1c,d and Figure S3a, the g-$C_3N_4/CoMoS_2$ heterojunction catalyst adopts a distinctive hierarchical architecture, with g-C_3N_4 nanosheets uniformly decorating the vertically aligned $CoMoS_2$ nanorods. This structural synergy leverages the complementary advantages of each component: the $CoMoS_2$ nanorods serve as robust scaffolds and efficient electron transport channels, while the g-C_3N_4 nanosheets, with their enlarged active surface area, enhance catalytic activity. The integration of g-C_3N_4 nanosheets onto $CoMoS_2$ nanorods effectively suppresses

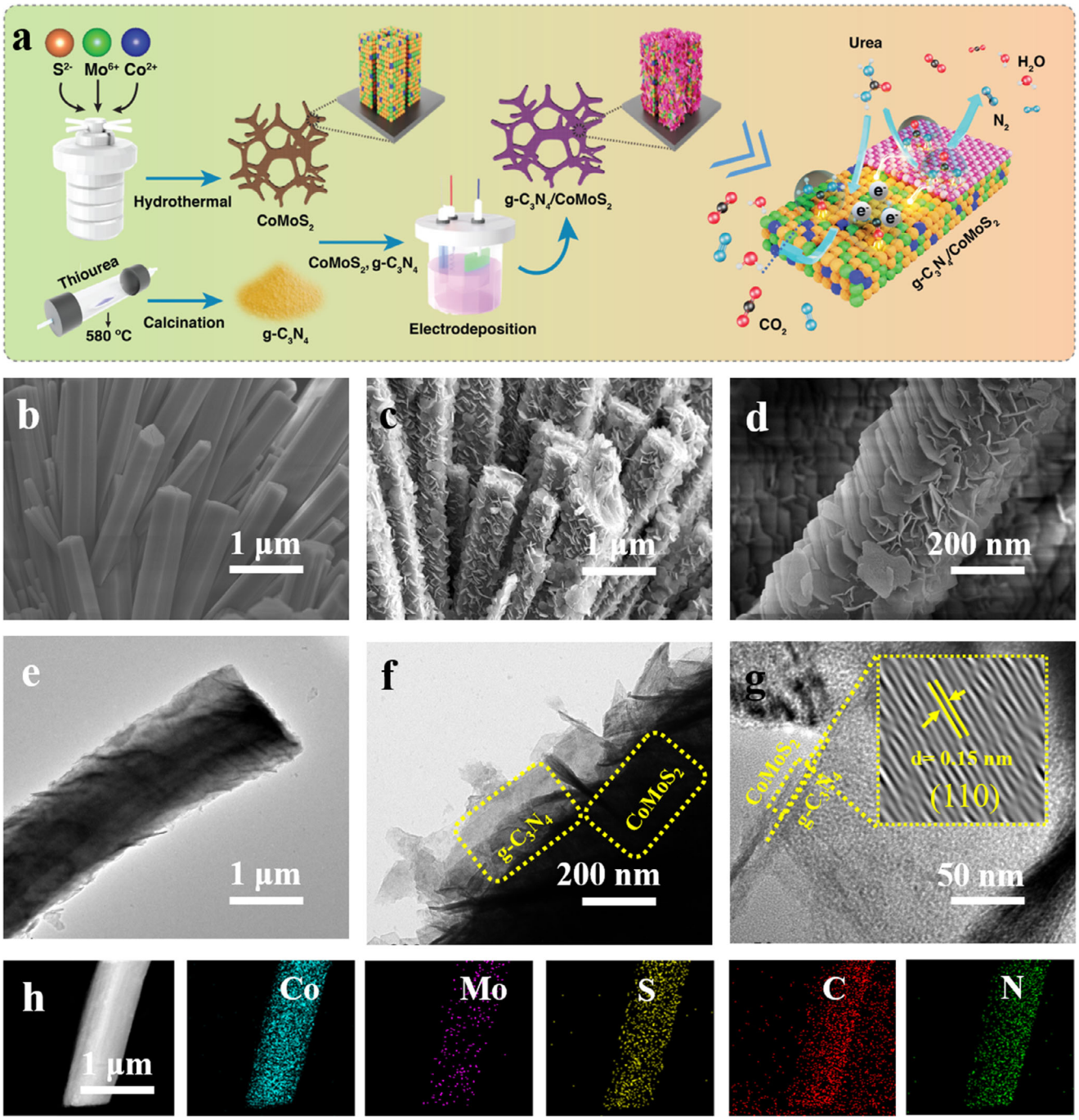

FIGURE 1 | Synthesis and morphological characterization of the g-C_3N_4/$CoMoS_2$ interface catalyst. (a) Schematic representation of the fabrication process of the g-C_3N_4/$CoMoS_2$ catalyst. Representative SEM images of (b) $CoMoS_2$ and (c,d) g-C_3N_4/$CoMoS_2$. (e,f) TEM images and (g) high-resolution TEM (HR-TEM) image of g-C_3N_4/$CoMoS_2$. (h) High-angle annular dark-field scanning TEM (HAADF-STEM) image along with corresponding elemental mapping of the g-C_3N_4/$CoMoS_2$ catalyst, confirming the uniform distribution of constituent elements.

material aggregation and detachment, thereby supporting long-term catalytic stability. TEM was employed to probe the fine structural features of the heterojunction. TEM images (Figure 1e,f and Figure S3b) show that the initially smooth $CoMoS_2$ nanorods are uniformly coated with g-C_3N_4 nanosheets. Fourier-transformed high-resolution TEM (**HRTEM**, Figure 1g) reveals clear lattice fringes with a spacing of 0.15 nm, corresponding to the (110) plane of $CoMoS_2$, confirming the heterostructure's high crystallinity without noticeable structural distortions. This atomic-level coupling at the g-C_3N_4/$CoMoS_2$ interface is expected to facilitate electronic communication and accelerate surface redox kinetics, enhancing electrocatalytic performance. High-angle annular dark-field scanning TEM (HAADF-STEM) combined with elemental mapping (Figure 1g) demonstrates a homogeneous distribution of Co, Mo, S, C, and N throughout the heterojunction. Collectively, these results confirm the successful fabrication of g-C_3N_4/$CoMoS_2$ via interface engineering, forming a well-defined heterojunction that expose abundant active sites, thereby boosting both HER and UOR performance [52].

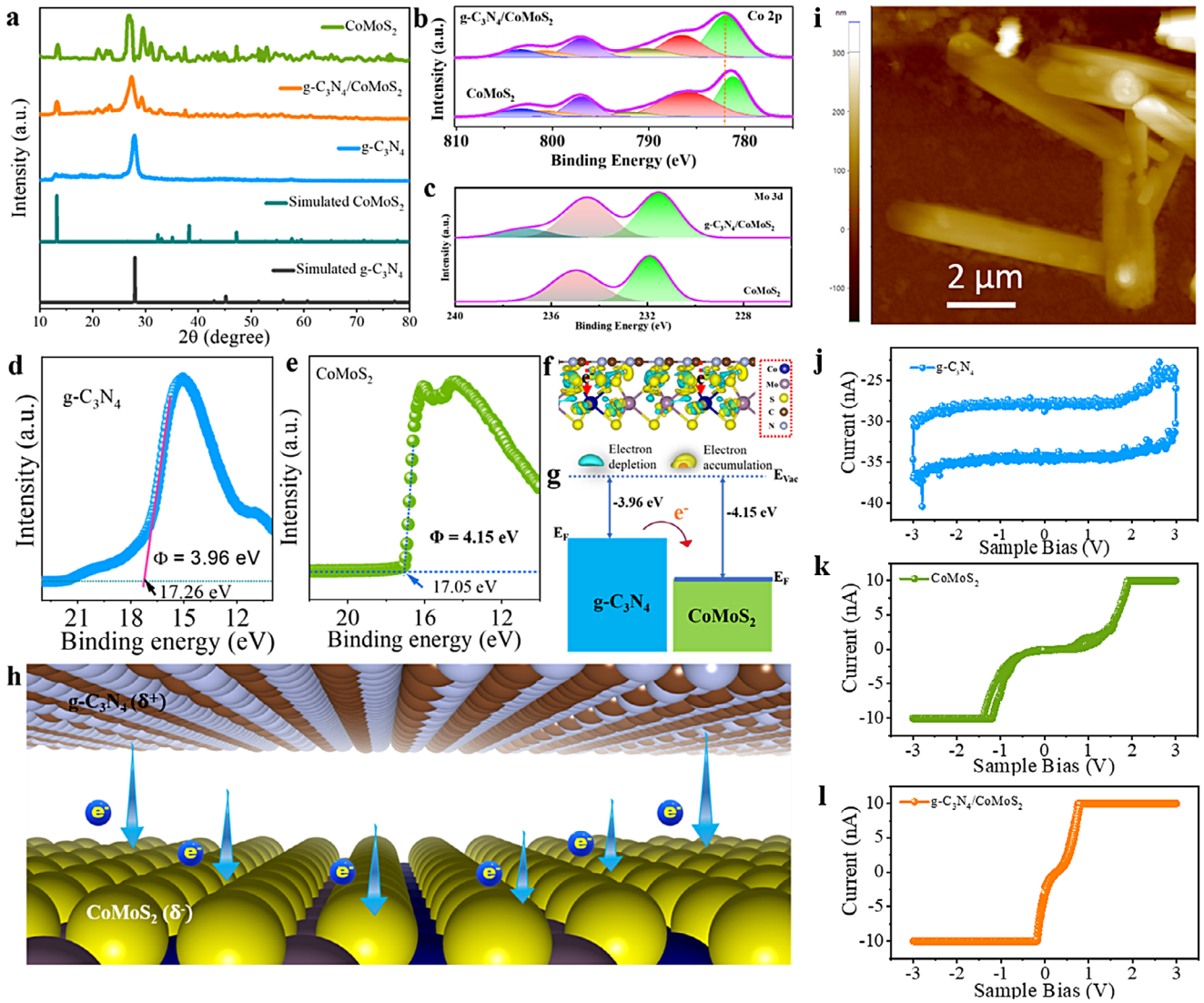

FIGURE 2 | Crystallographic and structural characterization, together with Conductive Atomic Force Microscopy (C-AFM) analysis, of the g-C_3N_4/$CoMoS_2$ interface and its associated charge-transfer characteristics. (a) XRD patterns of g-C_3N_4, $CoMoS_2$, and g-C_3N_4/$CoMoS_2$ catalysts. High-resolution XPS spectra of (b) Co 2p and (c) Mo 3d. UPS spectra of (d) g-C_3N_4 and (e) $CoMoS_2$, showing their corresponding **Φ**. (f) Differential charge density of g-C_3N_4/$CoMoS_2$ heterojunction at equilibrium, with yellow and cyan isosurfaces (1.21×10^{-3} e $bohr^{-3}$) indicating electron accumulation and depletion, respectively, revealing directional electron transfer from g-C_3N_4 to $CoMoS_2$. g) **Φ** alignment between g-C_3N_4 and $CoMoS_2$. (h) Schematic of interfacial electron transfer between g-C_3N_4 and $CoMoS_2$. (i) Topographic Z-height current image of g-C_3N_4/$CoMoS_2$. Current-voltage curves using C-AFM of (j) g-C_3N_4, (k) $CoMoS_2$, and (l) g-C_3N_4/$CoMoS_2$ heterojunction.

X-ray diffraction (XRD) analysis of g-C_3N_4/$CoMoS_2$ and the pristine components g-C_3N_4 and $CoMoS_2$ (Figure 2a) reveals well-defined crystalline phases that are in excellent agreement with simulated structures, indicating high phase purity with negligible impurities. $CoMoS_2$ exhibits diffraction peaks consistent with its simulated hexagonal phase, while g-C_3N_4 shows a prominent (002) reflection at $2\theta = 27.5°$. The characteristic $CoMoS_2$ peaks at 14.2°, 32.6°, and 58.3° correspond to the (002), (100), and (110) planes, confirming its layered hexagonal structure. The XRD patterns of the g-C_3N_4/$CoMoS_2$ heterojunction display the distinct reflections of both g-C_3N_4 and $CoMoS_2$, corroborating the successful formation of the heterojunction and the effective anchoring of g-C_3N_4 nanosheets onto the $CoMoS_2$ nanorod surface. X-ray photoelectron spectroscopy (XPS) was employed to elucidate the surface composition, chemical states, and electronic configurations of g-C_3N_4, $CoMoS_2$, and their g-C_3N_4/$CoMoS_2$ heterojunction. The XPS survey spectra (Figure S5) show characteristic peaks corresponding to Co, Mo, S, N, and C, consistent with the elemental composition revealed by HAADF-STEM analysis. The high-resolution Co 2p XPS spectrum of $CoMoS_2$ (Figure 2b) was deconvoluted into two doublet peaks at 781.4 and 797.6 eV, along with characteristic shake-up satellite features. The first doublet peak at 781.4 and 786.3 eV can be assigned to Co^{3+}, while the second doublet peak at 797.6 and 803.25 eV corresponds to Co^{2+}, respectively [53, 54]. Relative to $CoMoS_2$, the Co 2p peak in g-C_3N_4/$CoMoS_2$ exhibits a positive shift of 0.5 eV, indicative of pronounced electron redistribution at the g-C_3N_4/$CoMoS_2$ interface [55]. The Mo 3d XPS spectrum (Figure 2c) reveals a pair of peaks located at 231.4 and 234.5 eV corresponding to Mo $3d_{5/2}$ and Mo $3d_{3/2}$ doublets. The Mo 3d

binding energy in g-C_3N_4/$CoMoS_2$ exhibits a negative shift of 0.4 eV relative to pristine $CoMoS_2$, reflective of an increased local electron density. Likewise, the deconvoluted S 2p spectrum in $CoMoS_2$ revealed a pair of peaks at binding energies of 160.95 and 162.10 eV, which can be assigned to the S $2p_{3/2}$ and S $2p_{1/2}$ of the Mo—S bonds (Figure S6). Compared to $CoMoS_2$, the S-2p of g-C_3N_4/$CoMoS_2$ shows a positive shift of approximately 0.3 eV (Figure S6), indicative of an increased local electron density. The observed change in binding energies following the formation of a heterojunction can be explained based on elemental interactions. In the g-C_3N_4/$CoMoS_2$ heterostructure, the nitrogen of g-C_3N_4 serves as an electron donor, and the heterojunction interface acts as an electron acceptor. This synergistic effect optimizes a directional charge transfer channel, resulting in enhanced electron density accumulation around the Co—Mo—S bond, which will create a charge redistribution between Co, Mo and S. The observed positive shift in the binding energy of Co 2p and S 2p and negative shift for Mo 3d of the g-C_3N_4/$CoMoS_2$ relative to that of pristine $CoMoS_2$ suggest electron deficiency Co and S and electron rich Mo, hence electrons are pushed toward the Mo. These XPS analyses unequivocally confirm the formation of a chemically coupled heterojunction and substantiate the presence of interfacial electronic synergy.

To quantitatively probe the textural architecture governing catalytic behavior, nitrogen adsorption-desorption isotherms and Brunauer–Emmett–Teller (BET) analyses were performed to determine the specific surface area and pore size distribution of the materials (Figure S7). All catalysts display typical type IV isotherms accompanied by H3 hysteresis loops, indicative of well-developed mesoporous architectures [56]. The intrinsic microporosity of g-C_3N_4 anchored on $CoMoS_2$ induces additional mesopores, resulting in a g-C_3N_4/$CoMoS_2$ heterojunction with a BET surface area more than three times higher than that of g-C_3N_4 and $CoMoS_2$, as shown in Table S1. The construction of the heterojunction substantially enlarged the surface area and pore volume, underscoring that interface engineering is pivotal for electronic modulation and improved surface accessibility.

The interfacial charge-transfer efficiency is intrinsically associated with the ease of electron extraction, which can be quantitatively described by the **Φ** [57]. The **Φ** of g-C_3N_4 and $CoMoS_2$ (Figure 2d,e) were determined from Ultraviolet Photoelectron Spectroscopy (UPS) using the equation

$$\Phi = h\upsilon - \left(E_{cutoff} - E_F \right) \quad (1)$$

where Φ is the work function of the material, $h\upsilon$is the photon energy of the UV source (typically 21.22 eV for He I radiation), E_{cutoff} is the secondary electron cutoff, and E_F is the Fermi level energy. Moreover, differential charge density analysis corroborates electron migration from g-C_3N_4 to $CoMoS_2$, leading to electron depletion on g-C_3N_4 and accumulation on $CoMoS_2$ (Figure 2f). Bader charge analysis indicates that approximately 1.64 e is transferred from g-C_3N_4 to $CoMoS_2$ across the g-C_3N_4/$CoMoS_2$ junction, demonstrating a strong degree of interfacial electronic coupling. Accordingly, the UPS analysis confirms that g-C_3N_4 (3.96 eV) possesses a lower **Φ** than $CoMoS_2$ (4.15 eV), driving spontaneous electron transfer from g-C_3N_4 to $CoMoS_2$ upon contact. This charge redistribution continues until the Fermi levels equilibrate, thereby establishing a built-in internal electric field across the heterointerface (Figure 2g,h). To gain microscopic insight into the enhanced electrocatalytic activity, conductive atomic force microscopy (C-AFM) was employed to probe the local conductivity of the g-C_3N_4/$CoMoS_2$ heterojunction. Topographic Z-height maps (Figure 2i) reveal that g-C_3N_4 nanosheets uniformly decorate the vertically aligned $CoMoS_2$ nanorods. Current mapping under forward and reverse bias further reveals distinct conduction characteristics among the materials. To isolate the intrinsic contribution of the g-C_3N_4 component, current–voltage (*I–V*) characteristics were probed by conductive atomic force microscopy on pristine g-C_3N_4 nanosheets (Figure 2j), revealing uniformly low currents across the entire bias window. *I–V* curves further reveal the distinct charge-transport characteristics of pristine $CoMoS_2$ (Figure 2k) compared with those of the g-C_3N_4/$CoMoS_2$ heterojunction (Figure 2l). The *I–V* characteristics of g-C_3N_4/$CoMoS_2$ heterojunction exhibit a steeper, more symmetric response than those of pristine $CoMoS_2$, indicating enhanced charge injection and suppressed local hysteresis due to the formation of robust interfacial transport pathways.

2.2 | Investigation of the Electrocatalytic Activity for the HER

To elucidate the structural advantages of g-C_3N_4/$CoMoS_2$ for HER, the electrocatalytic performance of g-C_3N_4, $CoMoS_2$, Pt/C, and g-C_3N_4/$CoMoS_2$ was systematically evaluated in 1.0 M KOH using a three-electrode configuration. As schematically illustrated in Figure 3a, the alkaline HER proceeds through adsorption and dissociation of water molecules into adsorbed H* intermediates on the catalytic surface (Volmer step), followed by their electrochemical desorption and H_2 formation (Heyrovsky step). The linear sweep voltammetry (LSV) polarization curves (Figure 3b) demonstrate that g-C_3N_4/$CoMoS_2$ exhibits outstanding HER activity, requiring an overpotential of only 80 mV to achieve 10 mA cm^{-2}, significantly lower than those of pristine g-C_3N_4(280 mV), $CoMoS_2$ (190 mV), and even commercial Pt/C (110 mV). To gain further insight into the intrinsic reaction kinetics, Tafel slopes derived from the corresponding polarization curves were analyzed (Figure 3c). The g-C_3N_4/$CoMoS_2$ heterojunction delivers a notably lower Tafel slope of 28.38 mV dec^{-1}, compared to g-C_3N_4 (62.43 mV dec^{-1}), $CoMoS_2$ (43.13 mV dec^{-1}), and Pt/C (35.5 mV dec^{-1}), confirming its accelerated reaction kinetics and indicating that the HER predominantly proceeds via the Volmer–Heyrovsky mechanism [58]. The overpotentials at various current densities (10, 50, and 100 mA cm^{-2}) are summarized in Figure 3d, further confirming the superior catalytic efficiency of the heterojunction.

Electrochemical impedance spectroscopy (EIS) was employed to elucidate the charge-transfer dynamics at the electrode-electrolyte interface [59, 60]. As shown in Figure 3e, g-C_3N_4/$CoMoS_2$ exhibits a substantially reduced charge-transfer resistance (R_{ct}) compared to g-C_3N_4, $CoMoS_2$, and Pt/C, indicating enhanced interfacial electron transport and superior catalytic kinetics. The electrochemically active surface area (ECSA) was further estimated by evaluating the double-layer capacitance (C_{dl}) from cyclic voltammetry in the non-faradaic region (Figure S8). The g-C_3N_4/$CoMoS_2$ heterojunction exhibits an impressive C_{dl} value of 1.49 mF cm^{-2}, surpassing that of g-C_3N_4 (0.91 mF cm^{-2})

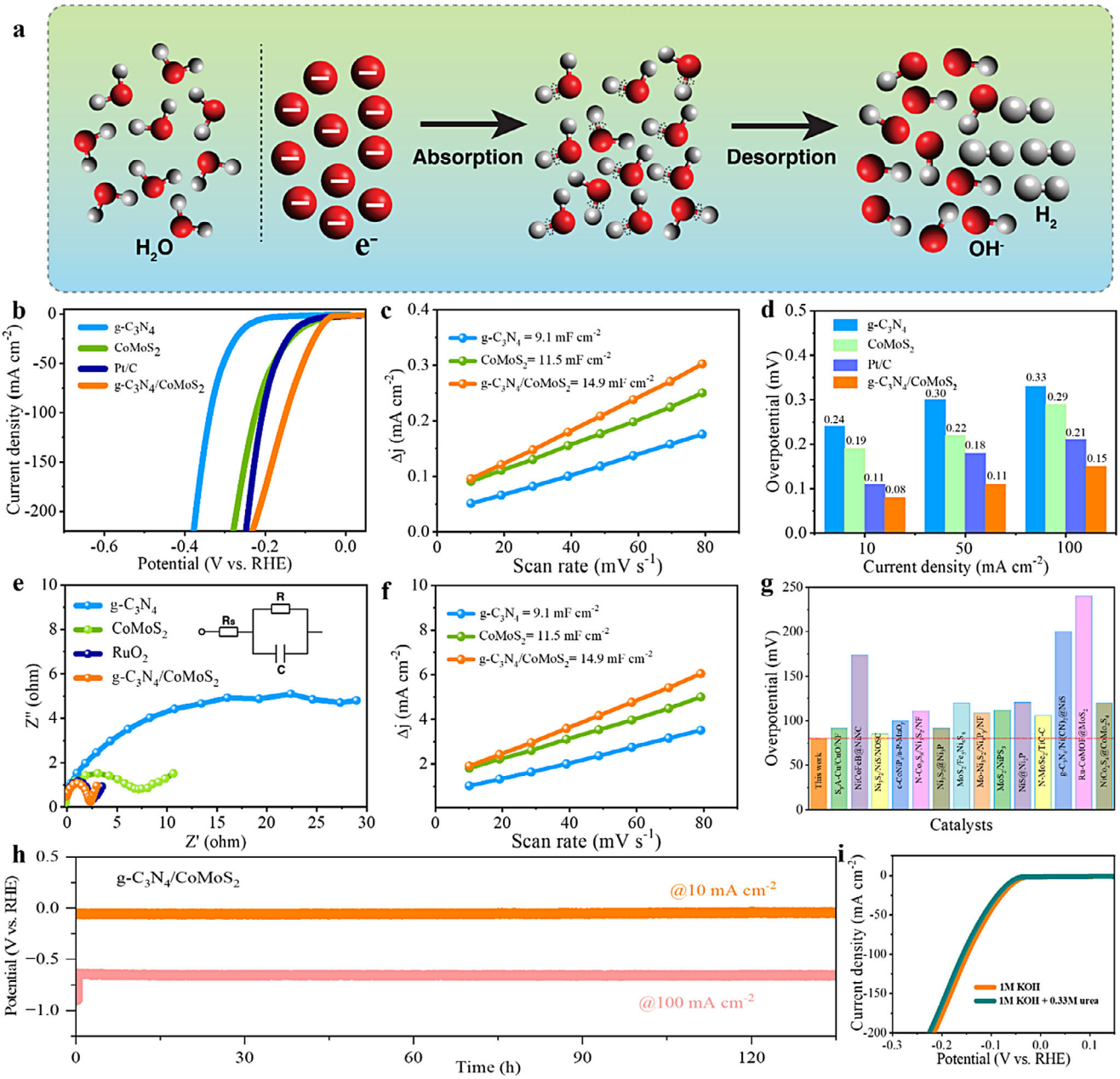

FIGURE 3 | Electrocatalytic activity for the HER in 1.0 M KOH Solution. (a) Schematic illustration of the HER mechanism. (b) LSV curves; (c) Tafel slopes; (d) Overpotentials at 10, 50, and 100 mA cm^{-2}; (e) Electrochemical impedance plots (Inset: equivalent circuit used in fitting the plot); (f) Calculated electrochemical double-layer capacitance values of g-C_3N_4, $CoMoS_2$, Pt/C, and g-C_3N_4/$CoMoS_2$. (g) Comparison of the g-C_3N_4/$CoMoS_2$ catalyst with previously reported materials. (h) Chronopotentiometric stability test at 10 and 100 mA cm^{-2}. (i) LSV curves of g-C_3N_4/$CoMoS_2$ in 1 M KOH electrolyte with and without 0.33 M urea.

and $CoMoS_2$ (1.15 mF cm^{-2}) (Figure 3f), implying a greater density of exposed active sites that facilitate enhanced hydrogen adsorption and accelerated HER kinetics. Furthermore, the g-C_3N_4/$CoMoS_2$ electrocatalyst demonstrates exceptional activity and durability, outperforming many recently reported non-noble-metal catalysts and ranking among the leading low-overpotential, high-stability systems (Figure 3g and Table S2). Long-term chronopotentiometric measurements at 10 and 100 mA cm^{-2} (Figure 3h) reveal negligible potential drift over 135 h of continuous operation, attesting to the excellent structural integrity and chemical robustness of the heterojunction catalyst. The post-test polarization curve (Figure S9) shows virtually no deviation from the initial measurement, confirming the outstanding durability and stability of the g-C_3N_4/$CoMoS_2$ heterojunction. Collectively, these comprehensive electrochemical evaluations affirm that the g-C_3N_4/$CoMoS_2$ heterojunction affords efficient charge transfer, abundant active sites, and durable catalytic interfaces. Finally, to establish continuity with preceding UOR studies, HER measurements were performed on g-C_3N_4/$CoMoS_2$ in 1 M KOH containing 0.33 M urea (Figure 3i). The negligible effect of urea on intrinsic HER activity indicates that, under practical operating conditions, UOR and HER can proceed simultaneously in a shared alkaline urea electrolyte, thereby simplifying system design and significantly reducing fabrication costs.

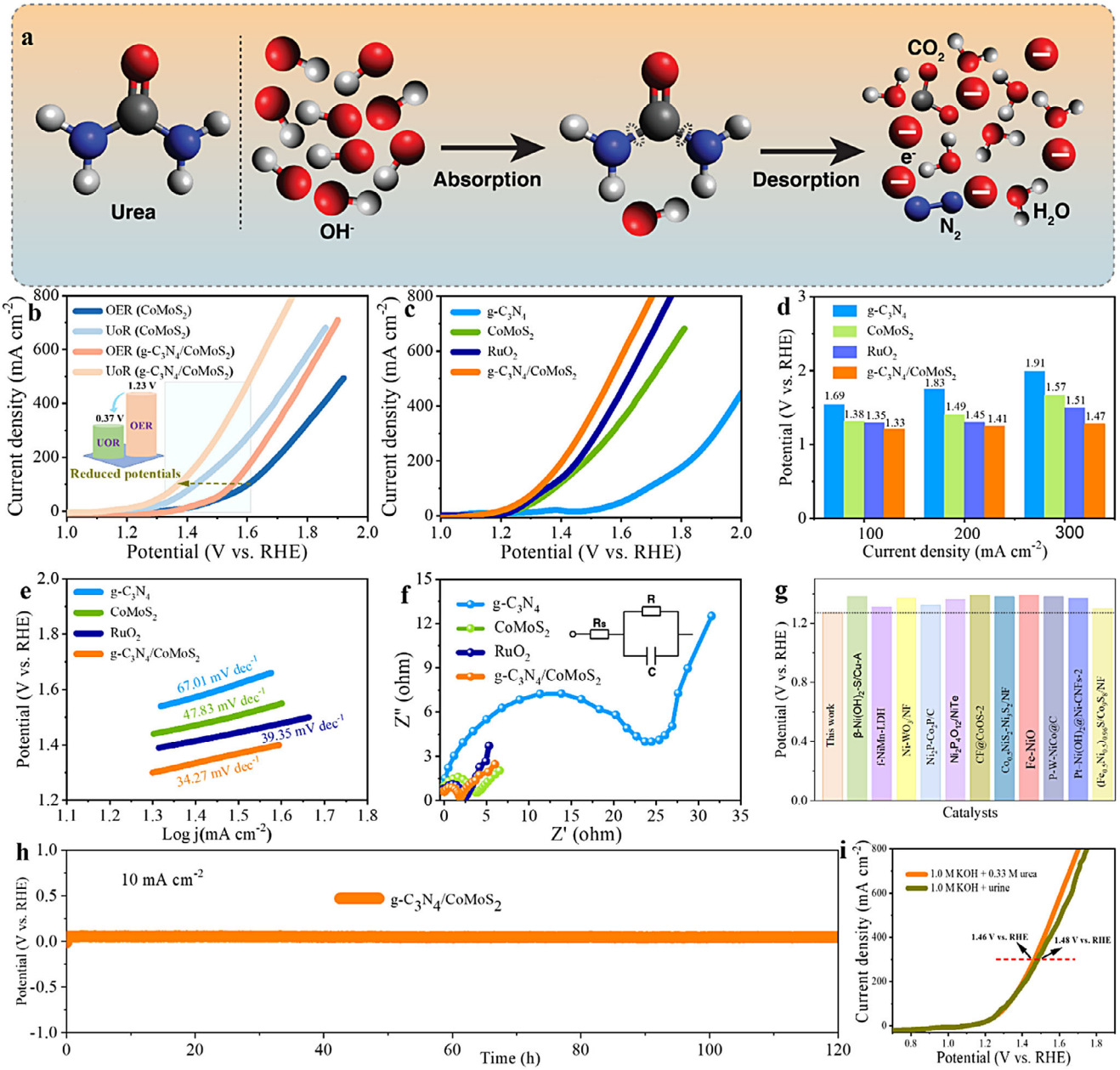

FIGURE 4 | UOR electrocatalytic performance and stability. (a) Schematic illustration of the UOR process. (b) Comparison of OER and UOR LSV curves for $CoMoS_2$ and g-C_3N_4/$CoMoS_2$ electrocatalysts. (c) LSV curves of UOR; (d) Potentials required to deliver current densities of 100, 200, 300 mA cm^{-2}; (e) Corresponding Tafel slopes; (f) Electrochemical impedance plots of the as-synthesized catalysts (Inset: equivalent circuit used in fitting the plot). (g) Comparison of the g-C_3N_4/$CoMoS_2$ catalyst with previously reported materials. (h) Chronopotentiometric stability test at 10 mA cm^{-2}. (i) LSV curves of g-C_3N_4/$CoMoS_2$ for UOR in 1.0 M KOH containing urine.

2.3 | Electrocatalytic UOR Performance

Considering that the anodic reaction dictates the overall rate of water electrolysis, the synthesized materials were employed as UOR anodes and systematically evaluated in a standard three-electrode setup at room temperature to elucidate their electrocatalytic behavior. As schematically depicted in Figure 4a, the UOR mechanism involves the initial adsorption of urea molecules on the catalyst surface, followed by their dissociation into key intermediates (*CO, *COOH, and *NH), wherein this dissociation step acts as the rate-determining process and consequently governs the overall efficiency of urea electrooxidation. The UOR performance of the g-C_3N_4/$CoMoS_2$ heterojunction was first evaluated in 1.0 M KOH under changing urea concentrations to uncover the concentration-dependent catalytic behavior. As presented in Figure S10, the well-defined g-C_3N_4/$CoMoS_2$ heterojunction efficiently catalyzes urea oxidation in alkaline media. The anodic current density exhibits a pronounced increase with rising urea concentration from 0.1 to 0.33 M, followed by a gradual decline at higher concentrations. This decrease is attributed to excessive urea molecules that hinder the accessibility of OH^- near the active sites, thereby suppressing C—N bond cleavage and limiting

the kinetics of UOR. LSV was performed to probe the competitive dynamics of urea oxidation and oxygen evolution in 1.0 M KOH, with and without 0.33 M urea. As depicted in Figure 4b, introducing urea markedly amplifies the anodic current density compared with OER and induces a clear leftward shift of the polarization curve. Specifically, g-C_3N_4/$CoMoS_2$ and $CoMoS_2$ require only 1.27 and 1.31 V, respectively, to achieve 10 mA cm^{-2}, whereas the corresponding OER potentials increase to 1.47 and 1.52 V. Figure 4c compares the LSV curves for g-C_3N_4/$CoMoS_2$, g-C_3N_4, $CoMoS_2$, and the benchmark RuO_2 in 1.0 M KOH containing 0.33 M urea, while OER measurements were conducted in 1 M KOH without urea (Figure S11). Notably, g-C_3N_4/$CoMoS_2$ exhibits the most pronounced UOR activity, delivering the lowest potential among all catalysts. Furthermore, this heterojunction requires significantly reduced overpotentials to achieve high current densities (100, 200, and 300 mA cm^{-2}) relative to the pristine components and RuO_2 (Figure 4d). Kinetic analysis based on Tafel slopes (Figure 4e) reveals that g-C_3N_4/$CoMoS_2$ heterojunction exhibits a markedly smaller slope (34.27 mV dec^{-1}) compared with g-C_3N_4 (67.01 mV dec^{-1}), $CoMoS_2$ (47.83 mV dec^{-1}), and RuO_2 (39.35 mV dec^{-1}), indicating more favorable reaction kinetics. EIS further confirms the enhanced charge-transfer properties of the heterojunction. As depicted in Figure 4f, g-C_3N_4/$CoMoS_2$ exhibits a significantly reduced charge-transfer resistance (R_{ct}), evidencing accelerated electron transport at the electrode/electrolyte interface.

As summarized in Figure 4g and Table S3, the g-C_3N_4/$CoMoS_2$ catalyst outperforms most recently reported UOR electrocatalysts. Beyond catalytic activity, long-term operational durability, a critical metric for industrial applicability, was assessed via chronopotentiometry. The g-C_3N_4/$CoMoS_2$ heterojunction exhibits outstanding stability, maintaining a constant potential with negligible activity loss over 120 h of continuous operation at 10 mA cm^{-2} (Figure 4h). The nearly overlapping LSV curves before and after the durability test (Figure S12) confirm the material's excellent electrochemical stability in 1 M KOH with 0.33 M urea. To elucidate the structural robustness of the catalyst, post-UOR characterizations, including XRD, XPS, and SEM (Figures S13–S15), were performed on g-C_3N_4/$CoMoS_2$. The consistent morphological, crystallographic, and surface chemical features observed after prolonged electrolysis confirm that the g-C_3N_4/$CoMoS_2$ heterojunction preserves its structural integrity and interfacial stability under extended operational conditions. Given the abundance of urea in domestic and industrial effluents, the electrocatalytic performance of g-C_3N_4/$CoMoS_2$ was assessed under practical conditions using human urine in 1.0 M KOH as the electrolyte for urea oxidation. As shown in Figure 4i, the catalyst achieves a current density of 300 mA cm^{-2} at a relatively low potential of 1.48 V vs. RHE, highlighting its outstanding activity in real urine. Compared with its performance in a standard 1.0 M KOH + 0.33 M urea electrolyte (1.46 V vs. RHE), the working potential in urine is slightly elevated, likely due to the presence of inorganic salts and other impurities, which can impede charge transfer and modestly reduce overall UOR efficiency. Stability was further evaluated under practical conditions using KOH with human urine as the electrolyte. The g-C_3N_4/$CoMoS_2$ heterojunction sustains a stable potential at 100 mA cm^{-2} over 120 h with negligible performance decay (Figure S16), underscoring its remarkable electrochemical resilience. Such stability reflects a pronounced resistance to chloride-induced corrosion and a high tolerance toward complex organic constituents in urine. This robustness is ascribed to the well-integrated heterointerface and finely tuned electronic coupling, which collectively preserve active site integrity and mitigate surface poisoning.

In view of the above results, Scheme 1 provides a schematic depiction of the potential urea electrooxidation process on the g-C_3N_4/$CoMoS_2$ heterojunction surface. The spontaneous electron redistribution from g-C_3N_4 to $CoMoS_2$ generates an internal interfacial electric field, leading to electron-deficient (electrophilic) regions on g-C_3N_4 and electron-rich (nucleophilic) regions on $CoMoS_2$. During UOR, the electron-rich amino group of urea preferentially coordinates with the electrophilic sites of g-C_3N_4, while the electron-withdrawing carbonyl group interacts with the nucleophilic domains of $CoMoS_2$, guided by interfacial electrostatic interactions. This cooperative electronic modulation across the heterointerface facilitates the activation and cleavage of the C—N bonds. In parallel, the lower **Φ** of g-C_3N_4 within the g-C_3N_4/$CoMoS_2$ architecture promotes the rapid desorption of reaction intermediates, thereby further enhancing the kinetics of urea electrooxidation.

2.4 | In Situ Raman Spectroscopy

The electrochemical reaction process and the catalytic mechanism of UOR and OER were investigated using in situ Raman spectroscopy. Figure 5a–c shows the in situ Raman spectra of g-C_3N_4/$CoMoS_2$ in 1 M KOH solution with 0.33 M of urea, recorded at the potential range of 1.20–1.60 V (vs. RHE). Under the UOR, a pair of broad signals was observed between 400–580 cm^{-1} at a potential less than 1.40 V. These broad signal peaks split into strong doublet peaks at 453 and 565 cm^{-1} when the potential was increased beyond 1.35 V, which can be attributed to bending and stretching vibrations from Co—O, respectively, due to the formation of CoOOH [61]. Additionally, a single peak observed around 1000 cm^{-1} corresponds to the C—N stretching of urea, and this C—N stretching band continues to decrease in intensity with an increase in potential, suggesting amide bond oxidation in urea. The electrochemical formation of CoOOH and the rapid decrease in intensity of the C—N stretching band indicate the occurrence of electrochemical oxidation of Co species, as shown in Equation (2) and chemical step reaction of urea resulting in the cleavage of the C—N bond as depicted in Equation (3).

$$6Co(OH)_2\,(s) + 6OH^- \leftrightarrow 6CoOOH\ (s) + 6H_2O\,(l) + 6e^- \quad (2)$$

$$CO(NH_2)_2\ (aq) + 6CoOOH\ (s) + H_2O\ (l) \rightarrow N_2\ (g) + CO_2\ (g) + 6Co(OH)_2\ (s) \quad (3)$$

Under the condition of OER (Figure 5d–f), the typical characteristic peak of C—N stretch does not appear as expected, and the Raman peak arising from Co—O does not appear until the potential reaches 1.45 V, which indicates that UOR occurs at a lower potential, hence confirming more favourable than the OER under these conditions.

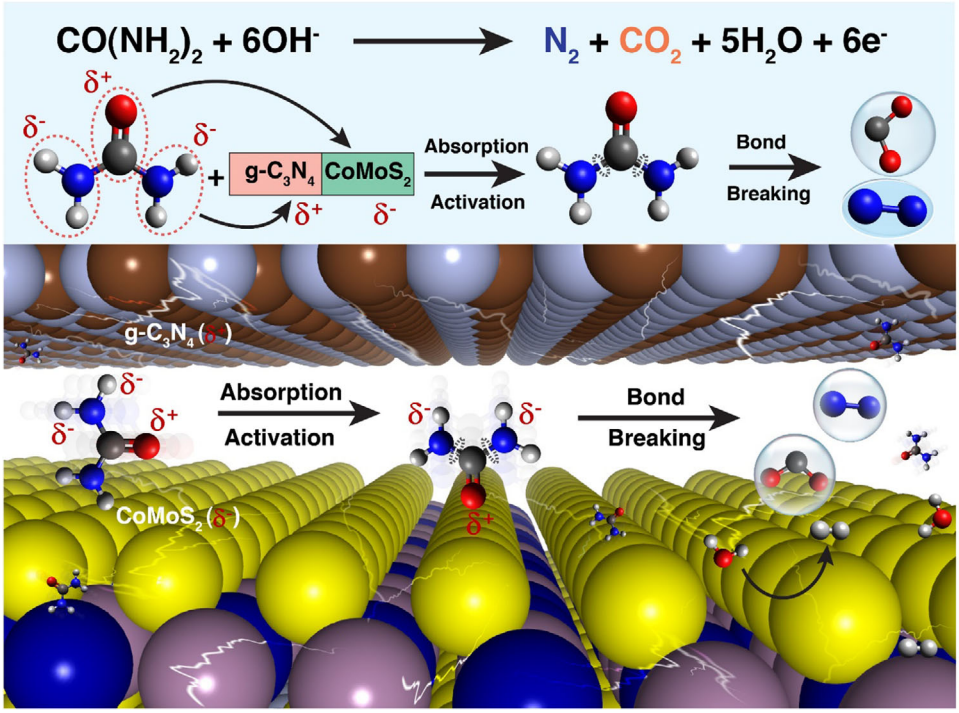

SCHEME 1 | Schematic of the proposed UOR mechanism at the g-C_3N_4/$CoMoS_2$ interface, indicating cooperative adsorption, electronic activation, and C—N bond cleavage to produce N_2 and CO_2.

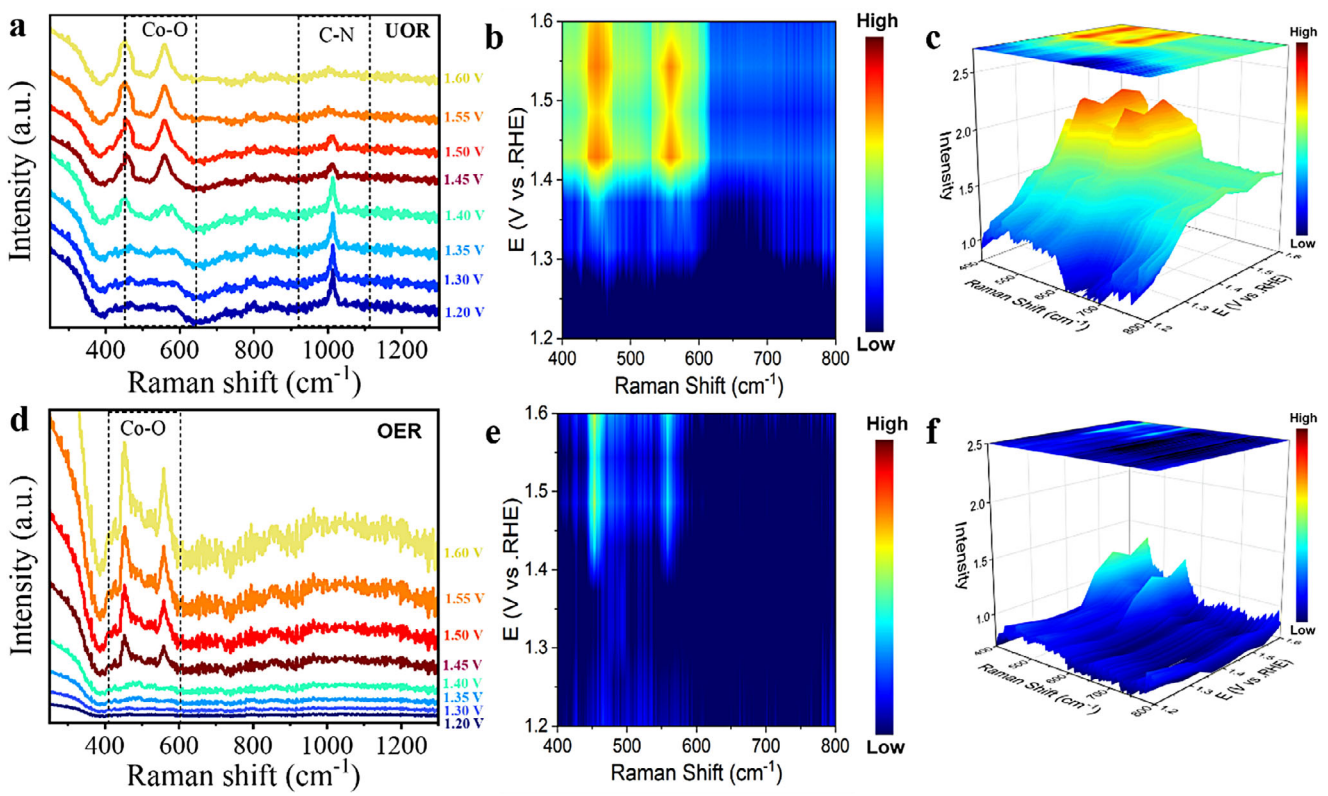

FIGURE 5 | Mechanistic insight. In situ Raman spectra with corresponding contour plots and in situ FTIR spectra of urea on g-C_3N_4/$CoMoS_2$ collected at different potentials during UOR (a–c) and OER (d–f).

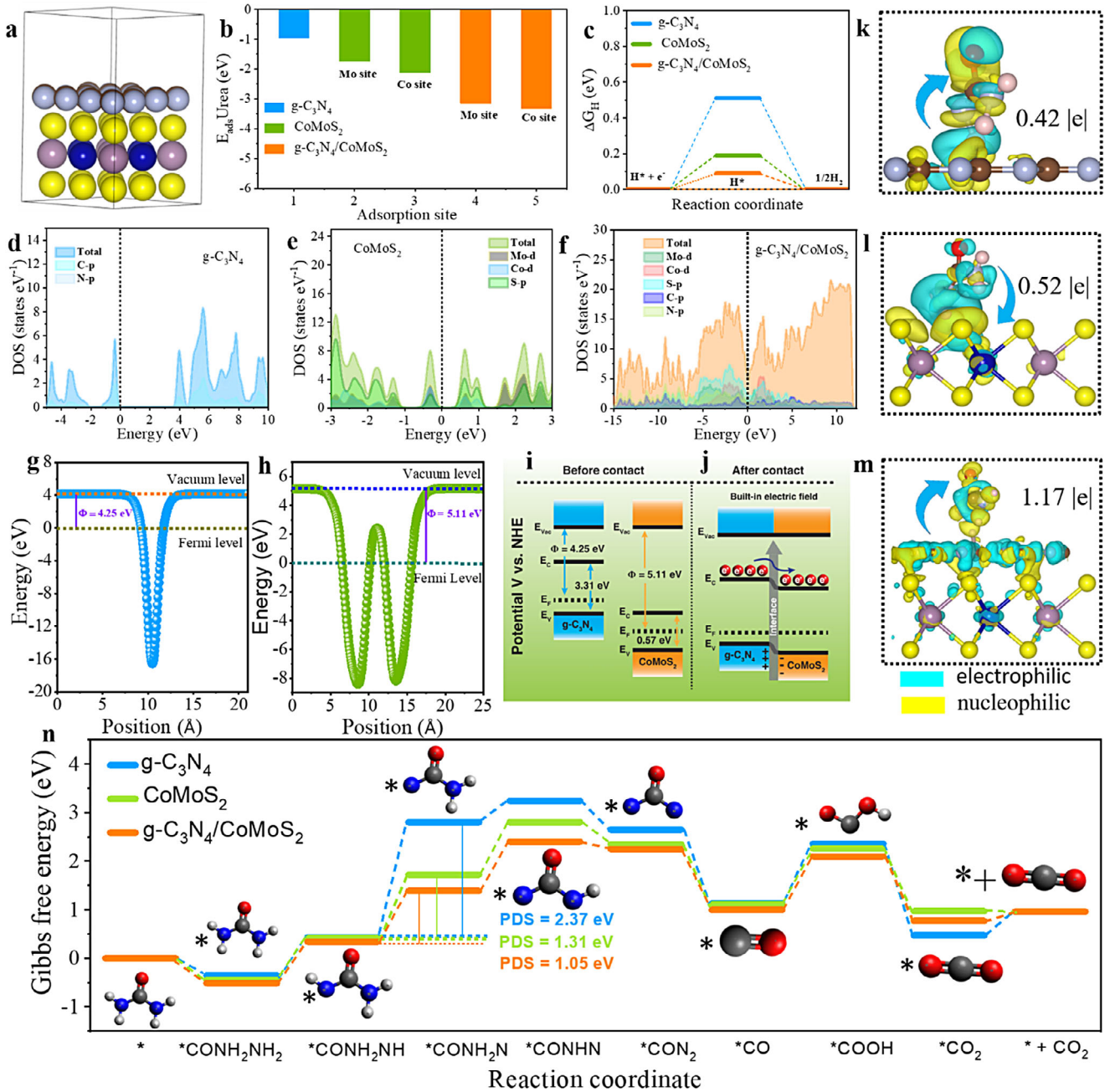

FIGURE 6 | DFT Insights into the Catalytic Mechanism. (a) Optimized structural model of the g-C_3N_4/$CoMoS_2$ heterojunction. (b) Comparison of the adsorption energies of urea on the metal sites within the heterojunction vs. those of its individual components. (c) The H-adsorption free energies of the g-C_3N_4/$CoMoS_2$ heterojunction and its individual components. DOS of (d) g-C_3N_4, (e) $CoMoS_2$, and (f) g-C_3N_4/$CoMoS_2$ heterojunction, with the Fermi level set as the reference (0 eV). The calculated **Φ** of (g) g-C_3N_4 and (h) $CoMoS_2$. Schematic illustrations of the band structures of g-C_3N_4 and $CoMoS_2$ (i) before and (j) after interfacial contact. Charge density differences and Bader charge analysis of adsorbed urea on (k) g-C_3N_4, (l) $CoMoS_2$, and (m) g-C_3N_4/$CoMoS_2$ heterojunction. (n) Theoretical free-energy profiles for the stepwise transformation of $CO(NH_2)_2$ into N_2 and CO_2 over g-C_3N_4, $CoMoS_2$, and the g-C_3N_4/$CoMoS_2$ heterojunction.

2.5 | DFT Calculations Predict the Mechanism of the UOR

To elucidate the mechanistic origin of the distinct UOR and HER pathways on the g-C_3N_4/$CoMoS_2$ heterojunction, density functional theory (DFT) calculations were conducted. As a reference, structural models of pristine g-C_3N_4 and $CoMoS_2$ were first established (Figure S17), while the optimized atomic configuration of the g-C_3N_4/$CoMoS_2$ heterojunction is presented in Figure 6a. Activation of adsorbed urea at catalytic sites is a prerequisite for initiating the UOR [62]. To elucidate its kinetic implications, urea adsorption was systematically evaluated on g-C_3N_4, $CoMoS_2$, and the corresponding heterojunction interface. To elucidate the catalytic active site, urea was adsorbed on the basal plane of g-C_3N_4 as well as the surface-exposed Co and Mo, and the adsorption energy was systematically calculated.

Representative structural configurations of urea adsorption at Co sites of $CoMoS_2$ and g-C_3N_4/$CoMoS_2$ are illustrated in Figure S18, and the corresponding adsorption energies at various active sites are summarized in Figure 6b. Urea binds weakly to g-C_3N_4 (−0.09 eV), but adsorption is substantially stronger at the Mo (−1.49 eV) and Co (−2.87 eV) sites of $CoMoS_2$. Integration of g-C_3N_4 with $CoMoS_2$ to form the g-C_3N_4/$CoMoS_2$ heterojunction yields the strongest urea adsorption, as evidenced by its markedly more negative adsorption energy (−2.80 eV), underscoring the enhanced surface affinity imparted by the heterointerface. The calculated urea adsorption energy is significantly lower than that of OH^- (1.24 eV) on the Co site of the heterojunction surface (Figure S19), indicating preferential urea adsorption and promoting UOR over OER, in agreement with the electrochemical observations. This thermodynamic preference reflects strengthened urea-surface interactions, facilitating the initial steps of UOR under alkaline conditions [22, 63]. Importantly, the Gibbs free energy of hydrogen adsorption (ΔG_{H^*}), key descriptor of HER activity, approaches the optimal value (≈ 0 eV) for efficient catalysts. The ΔG_{H^*} for g-C_3N_4/$CoMoS_2$ (0.09 eV) is substantially lower than that of g-C_3N_4 (0.51 eV) and $CoMoS_2$ (0.19 eV) (Figure 6c and Figure S20), highlighting its superior hydrogen adsorption [64]. Indeed, the lower ΔG_{H^*} for g-C_3N_4/$CoMoS_2$ corresponds to the experimental lower overpotential for HER. This enhancement arises from strong interfacial electronic coupling and optimized charge redistribution across the heterointerface, which collectively fine-tune the local electronic structure and facilitate proton reduction.

To assess the conductivity of the catalysts, electronic density of states (DOS) analyses were performed (Figure 6d–f). According to the DOS analysis, g-C_3N_4 and $CoMoS_2$ retain their distinctive semiconducting properties, with band gaps of approximately 3.31 and 0.57 eV, respectively. In contrast, the g-C_3N_4/$CoMoS_2$ heterojunction exhibits a markedly increased DOS near the Fermi level, indicative of enhanced electrical conductivity and accelerated charge-transfer kinetics. Such electronic synergy strengthens the coupling between the catalyst surface and reaction intermediates during UOR [65].

To probe the interfacial charge redistribution, the **Φ** of g-C_3N_4 and $CoMoS_2$ were determined to be 4.25 and 5.11 eV, respectively (Figure 6g,h), which is close to the experimentally observed **Φ** of 3.96 and 4.15 eV for g-C_3N_4 and $CoMoS_2$, respectively. The difference in **Φ** drives spontaneous electron transfer from g-C_3N_4 to $CoMoS_2$ until Fermi-level equilibrium is reached [63], as schematically illustrated in Figure 6i,j and Figure S21. This transfer results in electron depletion in g-C_3N_4 and accumulation in $CoMoS_2$, rendering the latter electron-rich. The resulting band alignment and built-in electric field across the g-C_3N_4/$CoMoS_2$ interface promote charge redistribution, where electron-enriched Co sites act as favorable adsorption centers for urea intermediates, thereby enhancing catalytic activity. To clarify the correlation between functional-group adsorption and catalytic performance, charge-density-difference and Bader-charge analyses were conducted for urea adsorption on g-C_3N_4, $CoMoS_2$, and the g-C_3N_4/$CoMoS_2$ heterojunction (Figure 6k–m). Bader analysis shows that urea acquires a more negative charge on g-C_3N_4/$CoMoS_2$ (−1.17 e) than on pristine g-C_3N_4 (−0.42 e) and $CoMoS_2$ (−0.52 e), indicating that the heterojunction enhances electron density on the adsorbed intermediate, which may facilitate stronger urea binding and lower the UOR overpotential, this observation corresponds to the experimental lower overpotential for UOR following heterojunction formation. To elucidate the complete reaction energetics, Gibbs free energy profiles were calculated for each catalytic system. As illustrated in Figure S22, the UOR proceeds through successive dehydrogenation and oxidation steps ($*CONH_2NH_2 \rightarrow *CONH_2NH \rightarrow *CONH_2N \rightarrow *CONHN \rightarrow * CON_2 \rightarrow *CO \rightarrow * COOH \rightarrow * CO_2 \rightarrow * + CO_2$) [66], consistent with previously established pathways. The corresponding free-energy diagrams for g-C_3N_4, $CoMoS_2$, and g-C_3N_4/$CoMoS_2$ (Figure 6n and Figures S23 and S24) reveal that the second dehydrogenation step ($*CONH_2NH \rightarrow *CONH_2N$) serves as the potential-determining step (PDS) for all catalysts [67]. Importantly, the g-C_3N_4/$CoMoS_2$ heterojunction exhibits a significantly reduced thermodynamic barrier of 1.05 eV compared with g-C_3N_4 (2.37 eV) and $CoMoS_2$ (1.31 eV), demonstrating that the heterojunction substantially lowers the reaction energy barrier. Collectively, these theoretical results confirm that heterojunction formation synergistically enhances both the kinetic and thermodynamic aspects of the UOR, consistent with the superior experimental performance of the g-C_3N_4/$CoMoS_2$ electrocatalyst.

2.6 | Performance of UOR-Assisted HER Bifunctional Electrodes

As schematically illustrated in Figure 7a, urea oxidation provides a thermodynamically and kinetically favorable anodic pathway, thereby substantially enhancing overall electrolysis efficiency. Accordingly, a two-electrode urea-assisted cell was constructed using g-C_3N_4/$CoMoS_2$ as both the anode and cathode in 1 M KOH containing 0.33 M urea (Figure 7b). The electrochemical behavior of g-C_3N_4/$CoMoS_2$ was first examined in this electrolyte configuration, with LSV curves recorded at scan rates from 5 to 50 mV s^{-1} (Figure 7c). The UOR activity remains essentially invariant across the entire scan-rate range, spanning both low- and high-current-density regimes, indicative of rapid charge-transfer kinetics and negligible capacitive contributions when the catalyst operates bifunctionally. For comparison, a conventional water electrolysis setup using g-C_3N_4/$CoMoS_2$//g-C_3N_4/$CoMoS_2$ in 1 M KOH was also examined. As shown in Figure 7d, the urea-assisted cell delivers a current density of 10 mA cm^{-2} at a cell voltage of only 1.34 V, markedly lower than the 1.70 V required for standard water electrolysis. Furthermore, the g-C_3N_4/$CoMoS_2$//g-C_3N_4/$CoMoS_2$ configuration achieves current densities of 10, 30, and 50 mA cm^{-2} at remarkably low cell voltages of 1.34, 1.38, and 1.41 V, respectively, significantly below the corresponding 1.70, 1.76, and 1.80 V required under OER conditions (Figure S25). Tafel slope analysis reveals distinct kinetics, with the HER//OER pair showing a slope of 114.63 mV dec^{-1}, notably higher than the 86.09 mV dec^{-1} for HER//UOR (Figure 7e). This highlights the kinetic benefits and enhanced hydrogen output of the HER//UOR pair, while avoiding the low-value oxygen produced in conventional electrolysis, offering a practical route for domestic wastewater treatment. The g-C_3N_4/$CoMoS_2$ cell also exhibits one of the lowest reported cell voltages for overall urea splitting at 10 mA cm^{-2} (Figure 7f). Finally, the g-C_3N_4/$CoMoS_2$ stability under UOR//HER current was evaluated. Under continuous

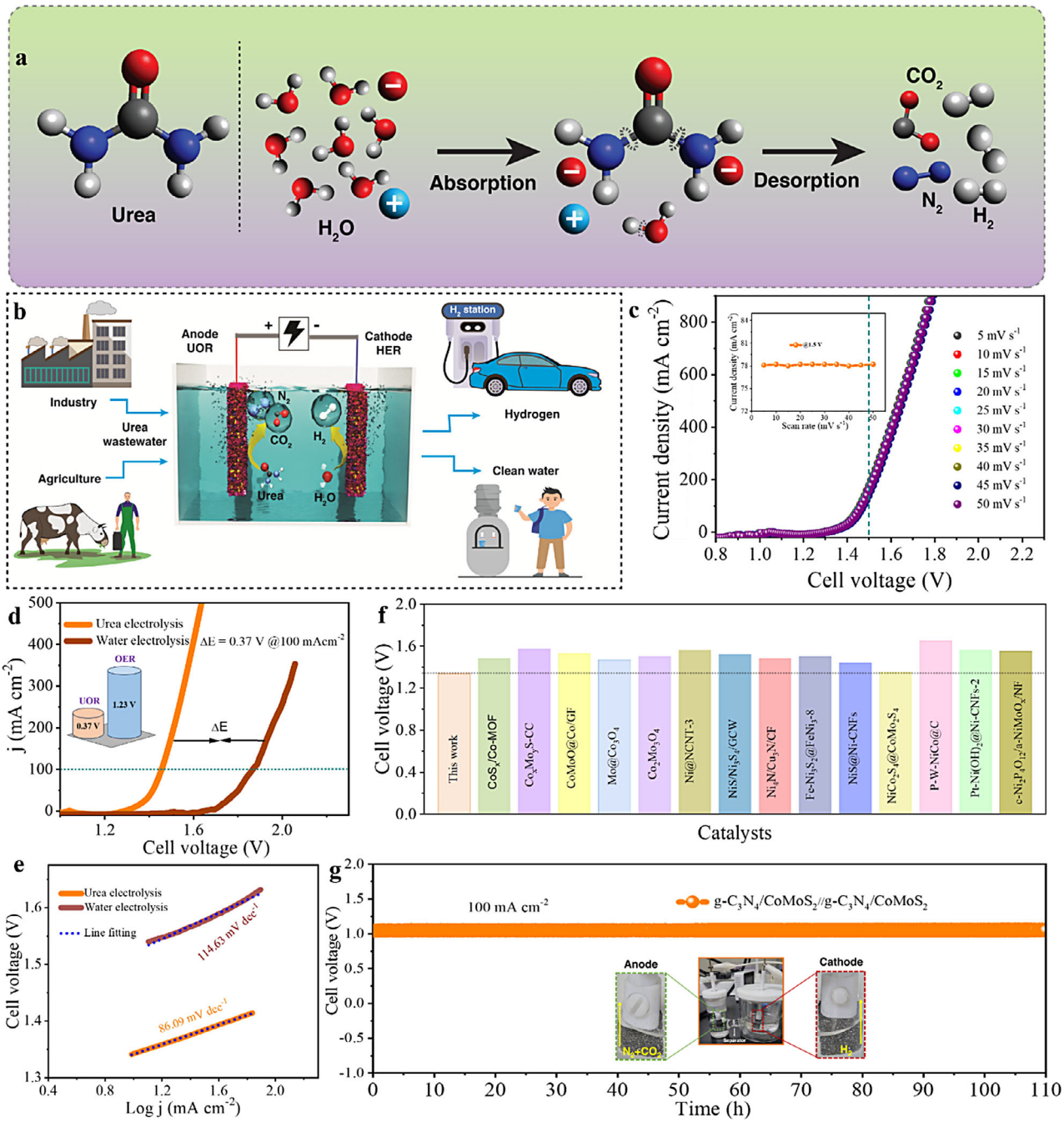

FIGURE 7 | Electrocatalytic activity and durability of the UOR//HER system in 1.0 M KOH with 0.33 M urea. (a) Schematic representation of H_2 production via urea-assisted water splitting. (b) Schematic illustration of the overall urea electrolysis process. (c) LSV curves of g-C_3N_4/$CoMoS_2$ at different scan rates (inset shows the corresponding current densities at 1.50 V with different scan rates). (d) LSV curves of g-C_3N_4/$CoMoS_2$ measured in 1.0 M KOH with and without 0.33 M urea. (e) Tafel slopes corresponding to the two LSV curves of the UOR||HER system in 1.0 M KOH with and without 0.33 M urea. (f) Cell voltages at 10 mA cm^{-2} for g-C_3N_4/$CoMoS_2$ as both anode and cathode were compared with those of other reported transition-metal-based bifunctional electrocatalysts. (g) Long-term electrochemical stability of g-C_3N_4/$CoMoS_2$ as both anode and cathode.

electrolysis at 100 mA cm^{-2} for 110 h, the catalyst exhibited negligible current fluctuations and maintained a stable potential, highlighting its exceptional long-term durability (Figure 7g). To investigate the practical challenges posed by urine-derived wastewater contamination, we performed electrolytic treatment of authentic human urine. The LSV profiles for electrolysis in 1.0 M KOH containing human urine (Figure S26) show a cell voltage of 1.48 V at 100 mA cm^{-2}, indicating substantially enhanced performance relative to the 1.87 V required for water electrolysis.

3 | Conclusion

This study overcomes the sluggish kinetics of the UOR through heterointerface engineering, wherein a built-in electric field

accelerates the reaction pathway. A robust g-C_3N_4/$CoMoS_2$ heterojunction was constructed through a hydrothermal and electrodeposition approach, coupling g-C_3N_4 nanosheets with $CoMoS_2$ nanorods to yield an efficient bifunctional electrocatalyst for both HER and UOR. This architecture enhances stability, expands the electrochemically active surface area, and facilitates efficient charge transfer. The interfacial energy disparity between g-C_3N_4 and $CoMoS_2$ drives spontaneous electron transfer from g-C_3N_4 to $CoMoS_2$, inducing a built-in electric field that creates electrophilic sites on g-C_3N_4 and nucleophilic sites on $CoMoS_2$. Consequently, the heterojunction exhibits remarkable bifunctional performance, delivering potentials of −80 mV vs. RHE for HER and 1.27 V vs. RHE for UOR at 10 mA cm^{-2}, with rapid kinetics and exceptional stability surpassing most state-of-the-art catalysts. DFT calculations reveal that **Φ**-driven interfacial electronic coupling directs electron transfer from g-C_3N_4 to $CoMoS_2$, elucidating the synergistic interactions within the heterojunction that underpin its superior electrocatalytic performance. In particular, when employed in a two-electrode urea-assisted cell, the heterojunction achieves a current density of 10 mA cm^{-2} at an ultralow cell voltage of 1.34 V, markedly reducing the energy demand for sustainable hydrogen production. This work demonstrates that built-in electric fields at heterojunction interfaces modulate active-site electronics, enabling a noble-metal-free catalyst for energy-efficient urea-assisted hydrogen production and offering a general strategy for sustainable electrocatalyst design.

Acknowledgements

This work was supported by the National Research Foundation of Korea (NRF) grant funded by the Korea government (MSIT) number RS-2024-00333541.

Conflicts of Interest

The authors declare no conflicts of interest.

Data Availability Statement

The data that support the findings of this study are available on request from the corresponding author. The data are not publicly available due to privacy or ethical restrictions.

References

1. Q. Qian, X. He, Z. Li, et al., "Electrochemical Biomass Upgrading Coupled With Hydrogen Production Under Industrial-Level Current Density," *Advanced Materials* 35 (2023): 2300935, https://doi.org/10.1002/adma.202300935.

2. W. Tang, L. Zhang, T. Qiu, et al., "Efficient Conversion of Biomass to Formic Acid Coupled With Low Energy Consumption Hydrogen Production From Water Electrolysis," *Angewandte Chemie International Edition* 62 (2023): 202305843, https://doi.org/10.1002/anie.202305843.

3. Z.-F. Huang, S. Xi, J. Song, et al., "Tuning of Lattice Oxygen Reactivity and Scaling Relation to Construct Better Oxygen Evolution Electrocatalyst," *Nature Communications* 12 (2021): 3992.

4. L. Zhang, L. Wang, H. Lin, et al., "A Lattice-Oxygen-Involved Reaction Pathway to Boost Urea Oxidation," *Angewandte Chemie* 131 (2019): 16976–16981, https://doi.org/10.1002/ange.201909832.

5. M. M. Khalaf, H. M. Abd El-Lateef, A. H. Touny, M. Saleh, and I. M. Mohamed, "Electrocatalytic Performance of Inorganic Nanoflakes Nickel Phosphates Under Adjusted Synthetic Parameters Towards Urea and Methanol Oxidation in Alkaline media," *Microchemical Journal* 163 (2021): 105901.

6. S. Yin, S. Liu, Z. Wang, et al., "Methanol-Assisted Energy-Saving Hydrogen Production Over Defect-rich Perforated PdIn Bimetallene," *Chemical Engineering Journal* 435 (2022): 134711, https://doi.org/10.1016/j.cej.2022.134711.

7. T. Take, K. Tsurutani, and M. Umeda, "Hydrogen Production by Methanol–Water Solution Electrolysis," *Journal of Power Sources* 164 (2007): 9–16.

8. Y. Liu, J. Zhang, Y. Li, Q. Qian, Z. Li, and G. Zhang, "Realizing the Synergy of Interface Engineering and Chemical Substitution for Ni_3 N Enables its Bifunctionality Toward Hydrazine Oxidation Assisted Energy-Saving Hydrogen Production," *Advanced Functional Materials* 31 (2021): 2103673, https://doi.org/10.1002/adfm.202103673.

9. B. You, N. Jiang, X. Liu, and Y. Sun, "Simultaneous H 2 Generation and Biomass Upgrading in Water by an Efficient Noble-Metal-Free Bifunctional Electrocatalyst," *Angewandte Chemie International Edition* 55 (2016): 9913–9917, https://doi.org/10.1002/anie.201603798.

10. T. Matthews, S. P. Mbokazi, T. H. Dolla, et al., "Electrocatalyst Performances in Direct Alcohol Fuel Cells: Defect Engineering Protocols, Electrocatalytic Pathways, Key Parameters for Improvement, and Breakthroughs on the Horizon," *Small Science* 4 (2024): 2300057, https://doi.org/10.1002/smsc.202300057.

11. M. A. Abdelkareem, E. T. Sayed, H. Alawadhi, and A. H. Alami, "Synthesis and Testing of Cobalt Leaf-Like Nanomaterials as an Active Catalyst for Ethanol Oxidation," *International Journal of Hydrogen Energy* 45 (2020): 17311–17319, https://doi.org/10.1016/j.ijhydene.2020.04.156.

12. Y. Chen, A. Lavacchi, H. Miller, et al., "Nanotechnology Makes Biomass Electrolysis More Energy Efficient Than Water Electrolysis," *Nature Communications* 5 (2014): 4036, https://doi.org/10.1038/ncomms5036.

13. L. Dai, Q. Qin, X. Zhao, et al., "Electrochemical Partial Reforming of Ethanol Into Ethyl Acetate Using Ultrathin Co_3O_4 Nanosheets as a Highly Selective Anode Catalyst," *ACS Central Science* 2 (2016): 538–544, https://doi.org/10.1021/acscentsci.6b00164.

14. B. F. Banti, H. Kang, S. Asgaran, et al., "Ni $(CN)_2$@ NiS Anchored on Graphitic Carbon Nitride as an Advanced Functional Electrode for Self-Powered Hydrazine-Assisted Hydrogen Generation," *International Journal of Hydrogen Energy* 200 (2026): 152831, https://doi.org/10.1016/j.ijhydene.2025.152831.

15. C. Tang, R. Zhang, W. Lu, et al., "Energy-Saving Electrolytic Hydrogen Generation: Ni_2P Nanoarray as a High-Performance Non-Noble-Metal Electrocatalyst," *Angewandte Chemie International Edition* 56 (2017): 842–846.

16. S. Barwe, J. Weidner, S. Cychy, et al., "Electrocatalytic Oxidation of 5-(Hydroxymethyl)furfural Using High-Surface-Area Nickel Boride," *Angewandte Chemie International Edition* 57 (2018): 11460–11464, https://doi.org/10.1002/anie.201806298.

17. S.-K. Geng, Y. Zheng, S.-Q. Li, et al., "Nickel Ferrocyanide as a High-Performance Urea Oxidation Electrocatalyst," *Nature Energy* 6 (2021): 904–912, https://doi.org/10.1038/s41560-021-00899-2.

18. X. Gao, X. Bai, P. Wang, et al., "Boosting Urea Electrooxidation on Oxyanion-Engineered Nickel Sites via Inhibited Water Oxidation," *Nature Communications* 14 (2023): 5842, https://doi.org/10.1038/s41467-023-41588-w.

19. L. Wang, Y. Zhu, Y. Wen, et al., "Regulating the Local Charge Distribution of Ni Active Sites for the Urea Oxidation Reaction," *Angewandte Chemie International Edition* 60 (2021): 10577–10582, https://doi.org/10.1002/anie.202100610.

20. N. Nwaji, B. Fikadu, M. Osial, et al., "Advanced Functional $NiCo_2S_4$@$CoMo_2S_4$ Heterojunction Couple as Electrode for Hydrogen Production via Energy-Saving Urea Oxidation," *Small* 21 (2025): 2410848, https://doi.org/10.1002/smll.202410848.

21. N. K. Shrestha, S. A. Patil, A. S. Salunke, A. I. Inamdar, and H. Im, "Unprecedented Urea Oxidation on Zn@Ni-MOF With an Ultra-High Current Density: Understanding the Competition Between UOR and OER, Catalytic Activity Limitation and Reaction Selectivity," *Journal of Materials Chemistry A* 11 (2023): 14870–14877, https://doi.org/10.1039/D3TA01962D.

22. G. Qian, J. Chen, W. Jiang, T. Yu, K. Tan, and S. Yin, "Strong Electronic Coupling of CoNi and N-Doped-Carbon for Efficient Urea-Assisted H_2 Production at a Large Current Density," *Carbon Energy* 5 (2023): 368, https://doi.org/10.1002/cey2.368.

23. X. Xu, H. Liao, L. Huang, et al., "Surface Reconstruction and Directed Electron Transport in $NiSe_2/MoSe_2$ Mott-Schottky Heterojunction Catalysts Promote Urea-Assisted Water Splitting," *Applied Catalysis B: Environmental* 341 (2024): 123312, https://doi.org/10.1016/j.apcatb.2023.123312.

24. Y. Zhou, B. Chu, Z. Sun, et al., "Surface Reconstruction and Charge Distribution Enabling Ni/W_5N_4 Mott-Schottky Heterojunction Bifunctional Electrocatalyst for Efficient Urea-Assisted Water Electrolysis at a Large Current Density," *Applied Catalysis B: Environmental* 323 (2023): 122168, https://doi.org/10.1016/j.apcatb.2022.122168.

25. B. Lu, Z. Li, J. Yin, K. Zhu, and K. Ye, "The $CoSe_2$ Hollow Cube/$CoSe_2$ Nanosheet Interface Catalyst for Efficient Electrolysis of Urea–Assisted Hydrogen Production at Industrial–Grade Currents," *Applied Catalysis B: Environment and Energy* 350 (2024): 123940, https://doi.org/10.1016/j.apcatb.2024.123940.

26. Z. Lv, Z. Li, X. Tan, et al., "One-step Electrodeposited NiFeMo Hybrid Film for Efficient Hydrogen Production via Urea Electrolysis and Water Splitting," *Applied Surface Science* 552 (2021): 149514, https://doi.org/10.1016/j.apsusc.2021.149514.

27. X. Xu, P. Du, T. Guo, B. Zhao, H. Wang, and M. Huang, "In situ Grown Ni phosphate@$Ni_{12}P_5$ Nanorod Arrays as a Unique Core–Shell Architecture: Competitive Bifunctional Electrocatalysts for Urea Electrolysis at Large Current Densities," *ACS Sustainable Chemistry & Engineering* 8 (2020): 7463–7471, https://doi.org/10.1021/acssuschemeng.0c01814.

28. X. Ao, Y. Gu, C. Li, et al., "Sulfurization-Functionalized 2D Metal-Organic Frameworks for High-Performance Urea Fuel Cell," *Applied Catalysis B: Environmental* 315 (2022): 121586, https://doi.org/10.1016/j.apcatb.2022.121586.

29. J. Wang, J. Wang, Y. Huang, D. Xu, and T. Tian, "Amorphous Iron-Doped Nickel Selenide Film on Nickel Foam via One-Step Electrodeposition Method for Overall Water Splitting," *Electrocatalysis* 14 (2023): 170–178, https://doi.org/10.1007/s12678-022-00780-0.

30. Z. N. Zahran, E. A. Mohamed, Y. Tsubonouchi, et al., "Electrocatalytic Water Splitting With Unprecedentedly Low Overpotentials by Nickel Sulfide Nanowires Stuffed Into Carbon Nitride Scabbards," *Energy & Environmental Science* 14 (2021): 5358–5365, https://doi.org/10.1039/D1EE00509J.

31. Y. Liu, B. Zhou, Y. Zhang, et al., "In Situ Synthesis of Two-dimensional Graphene-Like Nickel-Molybdenum Nitride as Efficient Electrocatalyst towards Water-Splitting Under Large-Current Density," *Journal of Colloid and Interface Science* 637 (2023): 104–111, https://doi.org/10.1016/j.jcis.2023.01.069.

32. S. Wen, J. Huang, T. Li, et al., "Multiphase Nanosheet-nanowire Cerium Oxide and Nickel-Cobalt Phosphide for Highly-efficient Electrocatalytic Overall Water Splitting," *Applied Catalysis B: Environmental* 316 (2022): 121678, https://doi.org/10.1016/j.apcatb.2022.121678.

33. X. Lv, S. Wan, T. Mou, et al., "Atomic-Level Surface Engineering of Nickel Phosphide Nanoarrays for Efficient Electrocatalytic Water Splitting at Large Current Density," *Advanced Functional Materials* 33 (2023): 2205161, https://doi.org/10.1002/adfm.202205161.

34. C. Zhang, X. Du, X. Zhang, and Y. Wang, "Ni_3S_2/M_xS_y–NiCo LDH (M = Cu, Fe, V, Ce, Bi) Heterostructure Nanosheet Arrays on Ni Foam as High-Efficiency Electrocatalyst for Electrocatalytic Overall Water Splitting and Urea Splitting," *Dalton Transactions* 52 (2023): 763–773, https://doi.org/10.1039/D2DT03047K.

35. S. Zheng, H. Qin, X. Cao, T. Wang, W. Lu, and L. Jiao, "Electron Modulation of Cobalt Carbonate Hydroxide by Mo Doping for Urea-assisted Hydrogen Production," *Journal of Energy Chemistry* 70 (2022): 258–265.

36. C.-J. Huang, H.-M. Xu, T.-Y. Shuai, Q.-N. Zhan, Z.-J. Zhang, and G.-R. Li, "A Review of Modulation Strategies for Improving Catalytic Performance of Transition Metal Phosphides for Oxygen Evolution Reaction," *Applied Catalysis B: Environmental* 325 (2023): 122313, https://doi.org/10.1016/j.apcatb.2022.122313.

37. Y. Mu, R. Ma, S. Xue, H. Shang, W. Lu, and L. Jiao, "Recent Advances and Perspective on Transition Metal Heterogeneous Catalysts for Efficient Electrochemical Water Splitting," *Carbon Neutralization* 3 (2024): 4–31, https://doi.org/10.1002/cnl2.105.

38. S. Xu, X. Ruan, M. Ganesan, J. Wu, S. K. Ravi, and X. Cui, "Transition Metal-Based Catalysts for Urea Oxidation Reaction (UOR): Catalyst Design Strategies, Applications, and Future Perspectives," *Advanced Functional Materials* 34 (2024): 2313309, https://doi.org/10.1002/adfm.202313309.

39. C.-J. Huang, Q.-N. Zhan, H.-M. Xu, H.-R. Zhu, T.-Y. Shuai, and G.-R. Li, "Fe-Doped $Ni_2P/NiSe_2$ Composite Catalysts for Urea Oxidation Reaction (UOR) for Energy-Saving Hydrogen Production by UOR-Assisted Water Splitting," *Inorganic Chemistry* 63 (2024): 8925–8937, https://doi.org/10.1021/acs.inorgchem.4c00985.

40. H. Tang, Z. Sun, S. Fan, et al., "Fe-Doped CoNi Layered Hydrogencarbonate Hierarchical Nano-Array Assisted Growth of ZIF-67 as an Efficient OER/UOR Bifunctional Catalyst Reaction for Overall Urea-Water Electrolysis," *Chemical Engineering Journal* 491 (2024): 152023, https://doi.org/10.1016/j.cej.2024.152023.

41. X. Li, Y. Wang, X. Du, and X. Zhang, "Controlled Synthesis of X (X = Mo, Cr, and W) Doped NiCoP Nanostructures as Efficient and Environmentally Friendly Urea Electrolysis Catalyst," *Fuel* 365 (2024): 131219, https://doi.org/10.1016/j.fuel.2024.131219.

42. J. Yan, L. Kong, Y. Ji, et al., "Single Atom Tungsten Doped Ultrathin α-$Ni(OH)_2$ for Enhanced Electrocatalytic Water Oxidation," *Nature Communications* 10 (2019): 2149, https://doi.org/10.1038/s41467-019-09845-z.

43. B. F. Banti, M. Goddati, N. Nwaji, et al., "Defect Engineered Ru-CoMOF@MoS_2 Heterointerface Facilitate Water Oxidation Process," *Chemsuschem* 18 (2025): 202402533, https://doi.org/10.1002/cssc.202402533.

44. Y. Liu, Z. Yang, Y. Zou, S. Wang, and J. He, "Trace Cobalt Doping and Defect Engineering of High Surface Area α-Ni $(OH)_2$ for Electrocatalytic Urea Oxidation," *Energy & Environmental Materials* 7 (2024): 12576, https://doi.org/10.1002/eem2.12576.

45. C. Fang, R. Li, X. Wang, et al., "Defect-Promoted Nanoparticles–Nanorod Ni–$NiMoO_4$ Heterogeneous Nanostructures as Efficient Electrocatalysts to Overall Water/Urea Splitting in Fresh/Sea Water," *Chemical Engineering Journal* 484 (2024): 149498, https://doi.org/10.1016/j.cej.2024.149498.

46. R. Ren, J. Wang, Y. Xie, et al., "Fe-Doping Accelerates the Reconstruction Kinetics of Metal-Organic Frameworks Toward Active Amorphous Oxyhydroxide Enabling Industrial Water Splitting," *Applied Catalysis B: Environment and Energy* 388 (2026): 126543, https://doi.org/10.1016/j.apcatb.2026.126543.

47. G. Zhao, K. Rui, S. X. Dou, and W. Sun, "Boosting Electrochemical Water Oxidation: The Merits of Heterostructured Electrocatalysts," *Journal of Materials Chemistry A* 8 (2020): 6393–6405, https://doi.org/10.1039/D0TA00708K.

48. Z. W. Seh, J. Kibsgaard, C. F. Dickens, I. Chorkendorff, J. K. Nørskov, and T. F. Jaramillo, "Combining Theory and Experiment in Electrocatalysis: Insights Into Materials Design," *Science* 355 (2017): aad4998, https://doi.org/10.1126/science.aad4998.

49. M. Yuan, J. Chen, Y. Bai, et al., "Electrochemical C–N Coupling With Perovskite Hybrids Toward Efficient Urea Synthesis," *Chemical Science* 12 (2021): 6048–6058.

50. S. Ni, H. Qu, Z. Xu, et al., "Interfacial Engineering of the $NiSe_2/FeSe_2$ p-p Heterojunction for Promoting Oxygen Evolution Reaction and Electrocatalytic Urea Oxidation," *Applied Catalysis B: Environmental* 299 (2021): 120638, https://doi.org/10.1016/j.apcatb.2021.120638.

51. M. He, C. Feng, T. Liao, S. Hu, H. Wu, and Z. Sun, "Low-Cost $Ni_2P/Ni_{0.96}S$ Heterostructured Bifunctional Electrocatalyst Toward Highly Efficient Overall Urea-Water Electrolysis," *ACS Applied Materials & Interfaces* 12 (2019): 2225–2233, https://doi.org/10.1021/acsami.9b14350.

52. P. Wang, P. Wang, T. Wu, C. Zhao, Z. Pu, and Y. Zhang, "Interface Engineering of $NiMoS_x$@NiMnFe Prussian Blue Analogue Nanowires to Efficiently Boost Overall Seawater Splitting at High Current Densities," *Advanced Functional Materials* 35 (2025): 2417924, https://doi.org/10.1002/adfm.202417924.

53. J. Li, G. Lu, G. Wu, et al., "Effect of TiO_2 Crystal Structure on the Catalytic Performance of Co_3O_4/TiO_2 Catalyst for Low-Temperature CO Oxidation," *Catalysis Science & Technology* 4 (2014): 1268–1275, https://doi.org/10.1039/C3CY01004J.

54. A. Muthurasu, S. S. Mers, and V. Ganesh, "Nitrogen Doped Graphene Quantum Dots (N-GQDs)/Co_3O_4 Composite Material as an Efficient bifunctional Electrocatalyst for Oxygen Evolution and Oxygen Reduction Reactions," *International Journal of Hydrogen Energy* 43 (2018): 4726–4737, https://doi.org/10.1016/j.ijhydene.2017.11.157.

55. J. Liu, J. Wang, B. Zhang, et al., "Mutually Beneficial Co_3O_4@MoS_2 Heterostructures as a Highly Efficient Bifunctional Catalyst for Electrochemical Overall Water Splitting," *Journal of Materials Chemistry A* 6 (2018): 2067–2072, https://doi.org/10.1039/C7TA10048E.

56. Í. Martínez-Visus, M. Ulcuango, B. Zornoza, J. Coronas, and C. Téllez, "Green and Fast Strategies for Energy-Efficient Preparation of the Covalent Organic Framework TpPa-1," *Chemistry–A European Journal* 29 (2023): 202203907.

57. D. Chen, R. Lu, R. Yu, et al., "Work-function-induced Interfacial Built-in Electric Fields in Os-$OsSe_2$ Heterostructures for Active Acidic and Alkaline Hydrogen Evolution," *Angewandte Chemie International Edition* 61 (2022): 202208642, https://doi.org/10.1002/anie.202208642.

58. J. Zhang, Y. Li, T. Zhu, et al., "3D Coral-Like $Ni_{10}S_2$ on Ni Foam as a Bifunctional Electrocatalyst for Overall Water Splitting," *ACS Applied Materials & Interfaces* 10 (2018): 31330–31339, https://doi.org/10.1021/acsami.8b09361.

59. A. Mariappan, P. Mannu, K. S. Ranjith, et al., "Novel Heterostructure-Based CoFe and Cobalt Oxysulfide Nanocubes for Effective Bifunctional Electrocatalytic Water and Urea Oxidation," *Small* 20 (2024): 2310112, https://doi.org/10.1002/smll.202310112.

60. R. K. Dharman, H. Im, M. K. Kabiraz, et al., "Stable 1T-MoS_2 by Facile Phase Transition Synthesis for Efficient Electrocatalytic Oxygen Evolution Reaction," *Small Methods* 8 (2024): 2301251, https://doi.org/10.1002/smtd.202301251.

61. Y. Bai, Y. Wu, X. Zhou, et al., "Promoting Nickel Oxidation state Transitions in Single-Layer NiFeB Hydroxide Nanosheets for Efficient Oxygen Evolution," *Nature Communications* 13 (2022): 6094, https://doi.org/10.1038/s41467-022-33846-0.

62. S. Lu, M. Hummel, S. Kang, et al., "Density Functional Theory Investigation of the NiO@Graphene Composite as a Urea Oxidation Catalyst in the Alkaline Electrolyte," *ACS Omega* 6 (2021): 14648–14654, https://doi.org/10.1021/acsomega.1c01758.

63. L. Li, X. Zhang, M. Humayun, et al., "Manipulation of Electron Spins With Oxygen Vacancy on Amorphous/Crystalline Composite-Type Catalyst," *ACS Nano* 18 (2023): 1214–1225, https://doi.org/10.1021/acsnano.3c12133.

64. Q. Zhou, C. Xu, J. Hou, et al., "Duplex Interpenetrating-Phase FeNiZn and $FeNi_3$ Heterostructure With Low-Gibbs Free Energy Interface Coupling for Highly Efficient Overall Water Splitting," *Nano-Micro Letters* 15 (2023): 95, https://doi.org/10.1007/s40820-023-01066-w.

65. S. Ye, F. Luo, Q. Zhang, et al., "Highly Stable Single Pt Atomic Sites Anchored on Aniline-stacked Graphene for Hydrogen Evolution Reaction," *Energy & Environmental Science* 12 (2019): 1000–1007, https://doi.org/10.1039/C8EE02888E.

66. X. Li, Y. Sun, J. Xu, et al., "Selective Visible-Light-Driven Photocatalytic CO_2 Reduction to CH_4 Mediated by Atomically Thin $CuIn_5S_8$ Layers," *Nature Energy* 4 (2019): 690–699, https://doi.org/10.1038/s41560-019-0431-1.

67. H. Ding, Z. Zhao, H. Zeng, et al., "Heterojunction-Induced Local Charge Redistribution Boosting Energy-Saving Hydrogen Production via Urea Electrolysis," *ACS Materials Letters* 6 (2024): 1029–1041, https://doi.org/10.1021/acsmaterialslett.3c01578.

Supporting Information

Additional supporting information can be found online in the Supporting Information section.

Supporting File: smll73842-sup-0001-SuppMat.docx.